

Article

Beam Test of the First Prototype of SiPM-on-Tile Calorimeter Insert for the EIC Using 4 GeV Positrons at Jefferson Laboratory

Miguel Arratia ^{1,2,*}, Bruce Bagby ¹, Peter Carney ¹, Jiajun Huang ¹, Ryan Milton ¹, Sebouh J. Paul ¹, Sean Preins ¹, Miguel Rodriguez ¹ and Weibin Zhang ¹

¹ Department of Physics and Astronomy, University of California, Riverside, CA 92521, USA

² Thomas Jefferson National Accelerator Facility, Newport News, VA 23606, USA

* Correspondence: miguel.arratia@ucr.edu

Abstract: We recently proposed a high-granularity calorimeter insert for the Electron-Ion Collider (EIC) that uses plastic scintillator tiles read out by SiPMs. Among its features are an ASIC-away-from-SiPM strategy for reducing cooling requirements and minimizing space use, along with employing 3D-printed frames to reduce optical crosstalk and dead areas. To evaluate these features, we built a 40-channel prototype and tested it using a 4 GeV positron beam at Jefferson Laboratory. The measured energy spectra and 3D shower shapes are well described by simulations, confirming the effectiveness of the design, construction techniques, and calibration strategy. This constitutes the first use of SiPM-on-tile technology in an EIC detector design.

Keywords: calorimeters; scintillators: scintillating fibres and light guides; scintillators: scintillation and light emission processes (solid, gas, and liquid scintillators); detector design: construction technologies and materials



Citation: Arratia, M.; Bagby, B.; Carney, P.; Huang, J.; Milton, R.; Paul, S.J.; Preins, S.; Rodriguez, M.; Zhang, W. Beam Test of the First Prototype of SiPM-on-Tile Calorimeter Insert for the EIC Using 4 GeV Positrons at Jefferson Laboratory. *Instruments* **2023**, *7*, 43. <https://doi.org/10.3390/instruments7040043>

Academic Editor: Antonio Ereditato

Received: 2 September 2023

Revised: 11 November 2023

Accepted: 13 November 2023

Published: 17 November 2023



Copyright: © 2023 by the authors. Licensee MDPI, Basel, Switzerland. This article is an open access article distributed under the terms and conditions of the Creative Commons Attribution (CC BY) license (<https://creativecommons.org/licenses/by/4.0/>).

1. Introduction

The future Electron-Ion Collider (EIC) [1] aims to explore nuclear structure and dynamics across a broad range of kinematics. In order to achieve this goal, a large acceptance detector called ePIC is being developed following the designs outlined in [2,3]. Maximizing acceptance in the ePIC central detector, which nominally spans the range of $-4.0 < \eta < 4.0$ in order to fulfill the EIC Yellow Report requirement [4], poses challenges due to the EIC's 25 mrad beam-crossing angle. This angle leads to a complex beampipe geometry, particularly in the vicinity of the ePIC forward calorimeter.

This challenge motivated the development of the high-granularity calorimeter insert (CALI) [5], specially designed to cover the range of $3.2 < \eta < 4.0$. As part of the forward hadronic calorimeter, the CALI needs to measure hadrons with an energy resolution better than $50\%/\sqrt{E} + 5\%$ [4]. The design incorporates absorber layers with unique shapes that accommodate the complex beampipe. Additionally, this design offers high granularity to enhance performance in measuring jets and effectively manage radiation damage (not in excess of 10^{12} neutrons/cm² per year at the highest luminosity [4]) and beam-gas interactions.

The CALI is based on Silicon Photo-Multiplier (SiPM) on-tile technology [6,7], offering flexibility, scalability, cost effectiveness, and high performance for high-granularity calorimeters [8]. In recent years, the SiPM-on-tile approach has become a popular option for various experiments [9–17]. A significant application of this technology is in the HGCAL upgrade for CMS at the high-luminosity LHC [17,18]. Numerous beam-test studies conducted by the CALICE Collaboration [8], as well as more recent studies by the CMS Collaboration [19,20], have provided invaluable references for new designs.

Unlike the current designs of the CMS HGCAL [17] and CALICE AHCAL [10], the CALI will have its ASIC readout chips at the back of the device, up to a meter away from

the SiPMs, instead of directly on them, a configuration that more closely resembles the early CALICE designs in [9,21]. This configuration results from constraints and limitations on the longitudinal space inside the ePIC detector. Among other factors, these prevent the use of in-detector cooling, which would be essential if the ASIC were placed directly within the detector. These chips, likely modified versions of the CMS HGROC ASIC [22], will obtain SiPM pulses via PCB, as initially proposed in [5]. The PCB will serve as a shielded cable that runs longitudinally to the back of the calorimeter.

The CALI will cover an area of about $60 \times 60 \text{ cm}^2$ and consist of 64 iron-scintillator layers, with each cell placed in 3D-printed frames that define a layer. This simultaneously holds the scintillator cells in place and reduces optical crosstalk between the cells [23]. Unlike the current CMS and CALICE designs [10,17], the entire layers of the CALI will be sandwiched between a pair of Enhanced Specular Reflector (ESR) foils, with the edges of the cells coated with reflective paint to increase the number of photons reaching the SiPM. Each layer will be positioned between a plastic cover and a PCB with SiPMs. This 3D-printed frame approach was introduced and tested on the bench in [23], and now, as reported here, has been tested under beam conditions for the first time.

In this paper, we present the outcomes of the first prototype built following the CALI design, with which a test-beam experiment was conducted with a positron beam at the Thomas Jefferson National Accelerator Facility (JLab). The objectives of this test were to validate the CALI design, in particular its incorporation of 3D-printed frames and the ASIC-away-from-SiPM approach, verify its simulations, assess its performance characteristics, refine the construction methods, and acquire experience in operating and calibrating the SiPM-on-tile detector.

This paper is structured as follows: Section 2 describes the prototype; Section 3 outlines the setup of the test beam; Section 4 details the data analysis; Section 5 presents the results; and Section 6 offers a summary.

2. Prototype

The first CALI prototype consisted of ten sampling layers, as illustrated in Figure 1, with a transverse active area of $9.5 \times 9.5 \text{ cm}^2$. Each steel block was 2 cm thick, corresponding to $1.1 X_0$, resulting in a total radiation length of $11.7 X_0$. The tiles were made of Bicon 404 plastic scintillator, each with a thickness of 6.2 mm and a dimple in its center. While CALI will use 3 mm thick tiles, we opted for this thickness because of the availability of the materials. The dimples were crafted using a CNC machine and subsequently hand-polished with sandpaper and NOVUS polishing liquid.

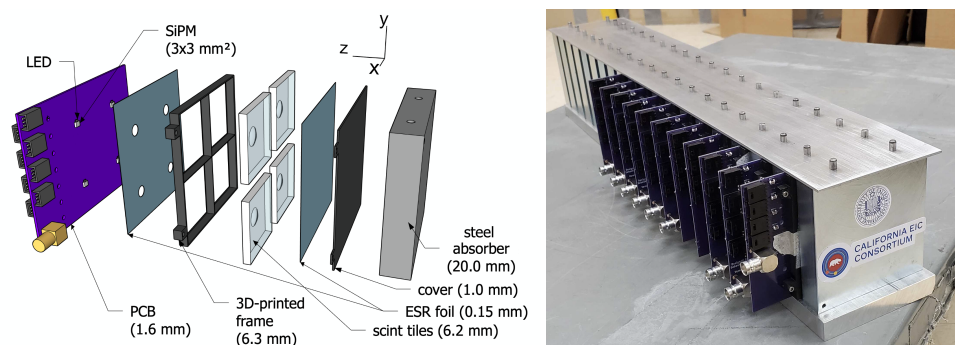


Figure 1. (Left): exploded view of prototype layer design. (Right): calorimeter insert prototype.

Following our earlier R&D efforts [23], we coated the edges of each cell with white reflective paint (Saint Gobain BC-621) and fit them into a plastic frame produced by an FDM 3D printer (Ender 3 V2 with a 0.4 mm nozzle size). The plastic frame had a width of 0.4 mm separating each scintillating tile from its neighbors in order to reduce optical crosstalk. The layers were sandwiched between 0.15 mm ESR foils; the layer of ESR foil in contact with the PCB had circular holes cut into it to promote coupling with the SiPM.

We employed a 1.6 mm PCB to mount the SiPMs and form the foundation of each layer, as illustrated in Figure 1. Each PCB had four SiPMs soldered onto it. We used the HPK S14160-3015PS SiPM, which has a $3 \times 3 \text{ mm}^2$ area and contains 39,984 pixels [24].

Among the ten sampling layers, the first four layers (0–3) included four square scintillator tiles, with each measuring 22 cm^2 . The last six layers (4–9) featured four hexagonal tiles, with each measuring 13 cm^2 . We tested both cell shapes for comparison purposes. Although the hexagonal tiles do not tessellate the area efficiently in this prototype, the CALI design has the potential to incorporate hexagonal tessellations with minimal or no dead area through the use of smaller cells [5] and a staggered design [25]. The centers of the dimples in the cells were aligned with the SiPMs on the boards within 1 mm, constrained by the dimensions of the cells and the frames that housed them.

With the scintillating tiles in place within the frames, the frames were fastened to a non-active region of the PCB extending from the left side of the prototype, as shown in Figure 1. Each of the sampling layers was then situated between the steel absorbers, again depicted in Figure 1. These absorbers were held in place by top and bottom plates linked with dowel pins. Lastly, the prototype was housed in a dark box made out of cardboard.

3. Experimental Setup and Data Acquisition System

The beam test was conducted in January 2023 at Hall D in JLab using positrons from the Pair Spectrometer (PS) of the GlueX experiment [26]. The data acquisition and trigger system was the CAEN FERS-5200 unit (model DT5202), and was entirely independent of the GlueX PS system. This configuration prevented us from using the PS hodoscope [27] for triggering and tagging the positron energy event-by-event. A 5 mm collimator was employed to restrict the beam profile vertically. Horizontally, the beam profile was fanned out as anticipated from a dipole-based pair spectrometer system; no collimator was used in this direction. We did not use a tracker system. The prototype's location and dimensions were used to estimate exposure to a beam with an energy range of approximately $4 \pm 1 \text{ GeV}$.

The FERS-5200 unit, which contains two CITIROC 1A ASICs, can independently bias and read out up to 64 SiPMs [28], and it additionally provides self-triggering capabilities. The CALI prototype PCBs are connected to the FERS-5200 unit through 1 meter of shielded cables using AMPMODU type 102241-1 connectors (CAEN A5261 [29]). This setup roughly mimics the ASIC-away-from-SiPM configuration to be used in the CALI design [5].

The FERS-5200 unit was set to operate in “spectroscopy mode”; upon triggering, it performs simultaneous acquisition across all channels using 13 bit analog-to-digital conversion and allows for a maximum trigger rate of 100 kHz. The trigger logic mandated that a minimum of four channels exceed a threshold of 220 ADC units (about 2.5 MIP for square cells); the trigger logic was configured with “MajorityLevel” set to 4, “TD_CoarseThreshold” at 220, and “QD_CoarseThreshold” at 250; the gain settings for both low and high gain were also set to 50. The SiPMs were biased at 43 V, which corresponds to an over-voltage of about 5 V. The readout data were synchronized to a laptop for storage and analysis. The max positron rate we observed was about 3 kHz, and we collected 6.2×10^5 trigger events.

4. Data Analysis

4.1. Pedestal and Cosmic Ray Runs

Dedicated pedestal runs obtained with random triggers in beam-off conditions were conducted to determine the pedestal mean position and widths for each channel independently. The ADC count spectrum in each channel was fitted to a Gaussian distribution. The average values of the pedestal means and widths were 59.6 ADC counts and 3.2 ADC counts, respectively.

Cosmic rays were used to calibrate the prototype on a channel-by-channel basis while defining the Minimum-Ionizing Particle (MIP) scale. Prior to the complete assembly in Hall D, the sampling layers were arranged in a vertical stack to maximize their exposure to cosmic rays. The layers were situated on top of each other in a modular 3D-printed rack. We conducted the cosmic ray collection overnight, using the same FERS-5200 settings

as in the beam test. The energy spectra, measured in ADC counts, were well-described by a Landau distribution. After subtracting the pedestal, the most probable value from a Landau fit was used as the MIP scale for each channel individually.

The MIP scale varied from channel to channel, falling within the range of approximately 55–70 ADC counts for the first four layers and 80–120 ADC counts for the subsequent six layers, with these ranges being associated with the larger square tiles and the smaller hexagonal tiles, respectively. The primary factor contributing to this discrepancy is likely the difference in area between the two tile shapes; a larger area results in a longer average path for a photon to reach the SiPM, leading to greater signal attenuation and consequently to a smaller light yield. The relatively wide fluctuation of MIP scale values within the same cell geometry can be attributed to inconsistencies in the polishing process or misalignments between the SiPM and the dimple.

4.2. Energy Calibration

No dedicated calibration at the SiPM pixel level was performed due to the limitation of the readout that was used. Nevertheless, benchtop measurements with different readout showed that the MIP scale for our prototype corresponds to approximately 60 pixels. Considering the maximum energy deposition of fewer than 100 MIPs, the SiPM saturation effect should not significantly impact our measurements.

The measured energy was calibrated from the ADC scale to the MIP scale as follows:

$$E_i[\text{MIP}] = \frac{(E_i[\text{ADC}] - \langle \text{pedestal} \rangle_i[\text{ADC}])}{\text{MPV}_i[\text{ADC}/\text{MIP}]} \quad (1)$$

Here, $E_i[\text{ADC}]$ is the measured charge for channel i in the ADC scale before pedestal subtraction, $\langle \text{pedestal} \rangle_i[\text{ADC}]$ is the pedestal mean for channel i , and $\text{MPV}_i[\text{ADC}/\text{MIP}]$ is the most probable value of the energy deposition for the i -th channel in ADC units obtained by MIP after pedestal subtraction.

4.3. Simulation

We used the DD4HEP framework [30] to simulate the response of the CALI prototype to positrons and muons. The version of GEANT4 [31] used within DD4HEP was 11.1.1, with the FTFP_BERT physics list and with Birks' constant set to 0.126 mm/MeV.

The simulated hits were digitized using a 13-bit ADC, incorporating the average and RMS pedestal values extracted from data without including any electronic or optical crosstalk or SiPM saturation effect. The MIP scale was determined based on the simulation of muons in a manner analogous to the way that it was determined in the data. In the simulation, the calibration constant was assumed to be identical for all channels.

The beam parameters in the simulation were tuned to match the beam conditions in the test beam. Due to the absence of a tracking system in our setup, we could not accurately determine the beam's direction. Analysis of the prototype data revealed a slope in the energy-weighted vertical shower position as a function of layer number, suggesting a beam tilt and a vertical shift relative to the prototype's center. To address this, we adjusted the shift distance and tilt angle to match the data. Our findings indicated a vertical misalignment and tilt polar angle of approximately 15 mm and $40 < \theta < 44$ mrad, respectively, as illustrated in Figure 2. The beam energy was parameterized to exhibit linear dependence on the horizontal position, as expected from the the pair spectrometer that generated the positrons:

$$E = E_0 + C \cdot x \quad (2)$$

where E_0 is the energy at the center of the prototype, which was tuned to be 4.2 GeV, x is the signed horizontal distance to the center position, and C reflects the dependence of the energy on the position, which was determined to be 177 MeV/cm. The resulting beam energy ranged from 3.3 GeV to 5.1 GeV across the prototype's front face, roughly aligning with expectations based on its location and transverse size. The beam intensity

was assumed to be uniform across this energy range, which we expect to be a reasonable approximation with respect to the PS spectra.

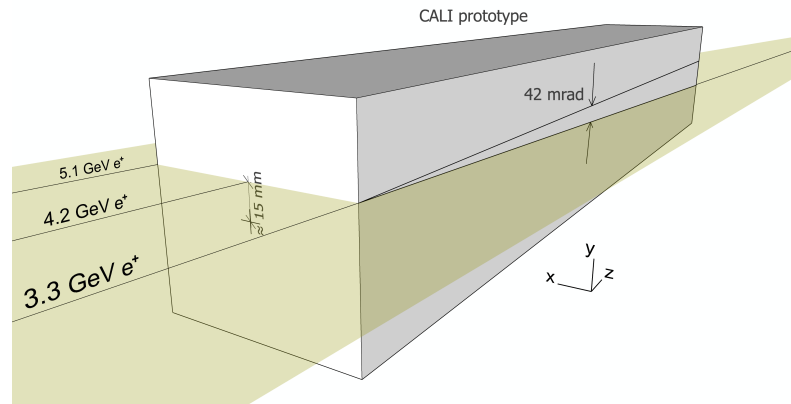


Figure 2. Relative position and tilt of the beam midplane in relation to the prototype, as identified by adjusting the simulation to align with the data. In addition, the figure indicates the energies of positrons that hit the prototype at the left edge, middle, and right edges of its front face.

4.4. Hit and Event Selection

The trigger logic used during data collection was imposed on our simulated dataset. In the following analysis, we consider only hits with $E > 0.3$ MIP and select only events with at least four hits above this threshold. The same hit and event selection criteria were applied in the simulation. This cut removed 0.2% of events from the data and 0.9% of events from the simulation. The difference reflects discrepancy in the descriptions of the rate of events with low hit multiplicity.

5. Results

Figure 3 presents the distribution of the number of hits above the $E > 0.3$ MIP threshold along with the hit-energy spectra. Most events show a hit multiplicity ranging between 10 and 20, with a peak at approximately 15 hits per shower in both the data and simulation. However, the simulation exhibits a broader distribution. The hit-energy spectra show that the energy of a single hit can reach up to 80 MIPs. A good agreement between the data and simulation is observed in the low-energy and mid-energy region, but not in the high-energy region.

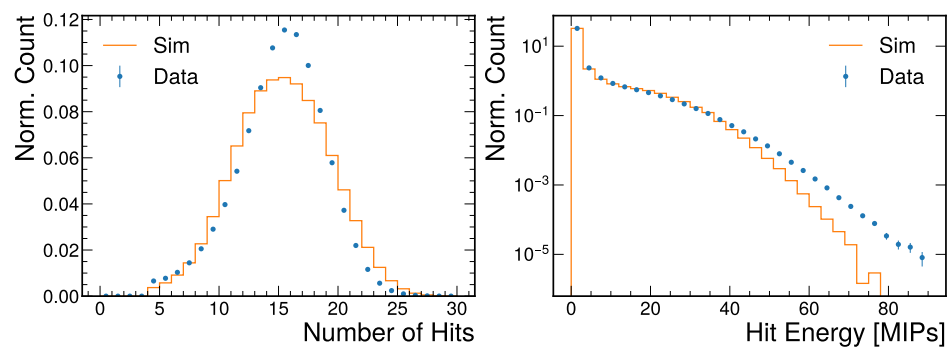


Figure 3. Number of hits above threshold per shower (left) and corresponding hit-energy spectrum (right).

The tilted and shifted beam condition is particularly noticeable in the observable Center of Gravity (COG), which is defined as a 3D vector and calculated event-by-event as follows:

$$\text{COG} = \frac{\sum_i E_i \cdot \vec{X}_i}{\sum_i E_i} \tag{3}$$

Here, the index i cycles through all hits with $E > 0.3$ MIP, E denotes the hit energy, and \bar{X}_i is the 3D position of the center of the tile where the i -th hit takes place. The horizontal, vertical, and longitudinal projections of the COG are presented in Figure 4. The transverse variables are expressed in units of cm, and the longitudinal variables are in units of radiation lengths.

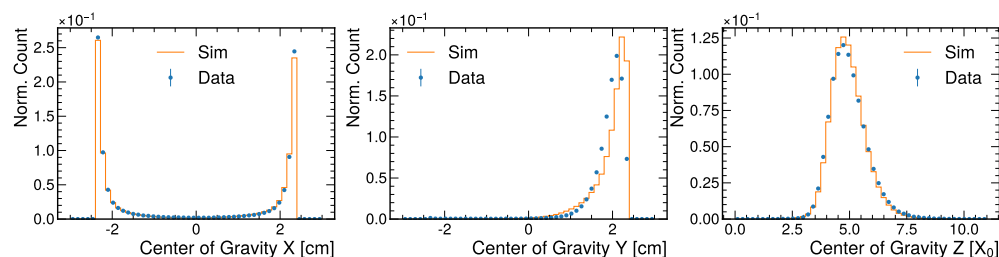


Figure 4. Shower center of gravity in horizontal (left), vertical (middle), and longitudinal (right) directions.

The COG_x distribution shows a nearly symmetrical pattern, a feature accurately captured by the simulation. In contrast, the COG_y distribution shows a single peak that suggests an upward shift in the beam's position, while the tail indicates a slight beam tilt. This distribution is not as well captured by the simulation, pointing to imperfections in modeling the beam directions. Meanwhile, the COG_z distribution has a Gaussian-like shape, peaking at around $5 X_0$ or approximately in the fourth layer, and is well described by the simulation.

Figure 5 displays the hit-energy spectra across all 40 channels. Most spectra are reasonably described by the simulation. Channels 1 and 7 were non-functional, likely due to lost cable connections during transport to the beam test area, and are masked in the simulation results. The prominent spikes in channels 16 and 17 were due to the saturation of the CAEN unit's ADC dynamic range; this effect was included in the simulated data as well.

Channels 9 and 16 show larger signals in the simulation than what is observed in the data. Considering that their horizontally symmetric counterparts, channels 8 and 17, align well with the simulation, a likely explanation for this discrepancy could be an incorrect MIP scale for these specific channels in the data. This variation in MIP scale could have resulted from the reassembly of the prototype between cosmic and beam runs, potentially shifting the tile positions relative to the SiPMs and affecting the light yields [32]. This misalignment might explain the discrepancies in channels 6 and 33. To address this, future tests will incorporate in situ cosmic runs to overcome this specific challenge if sufficient time is allocated.

In light of the reasonable agreement observed at the channel level, a similar level of congruence is anticipated at the layer level, as depicted in Figure 6. The most pronounced signals consistently occur in the first four layers. The kink observed in the distribution for layer 4 can be attributed to the ADC capacity limit effect observed in channels 16 and 17.

Figure 7 displays the median values and RMS of the energy distribution for each layer. The measured median values align closely with the simulation. The RMS of the layer energy is reasonably described as well, although the simulation results are somewhat smaller than those in the data.

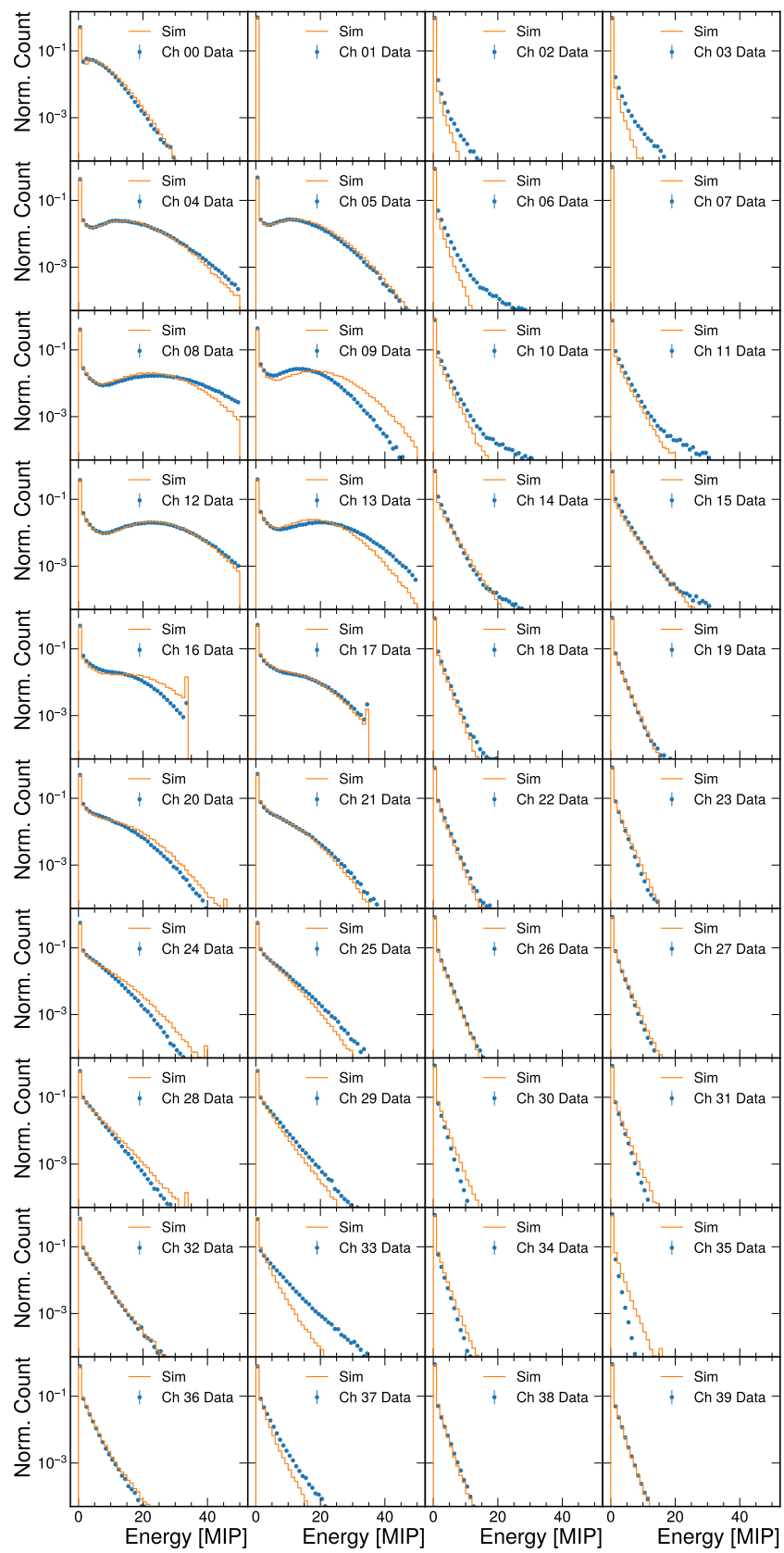


Figure 5. Energy spectra for each channel; each row represents a single layer in the detector.

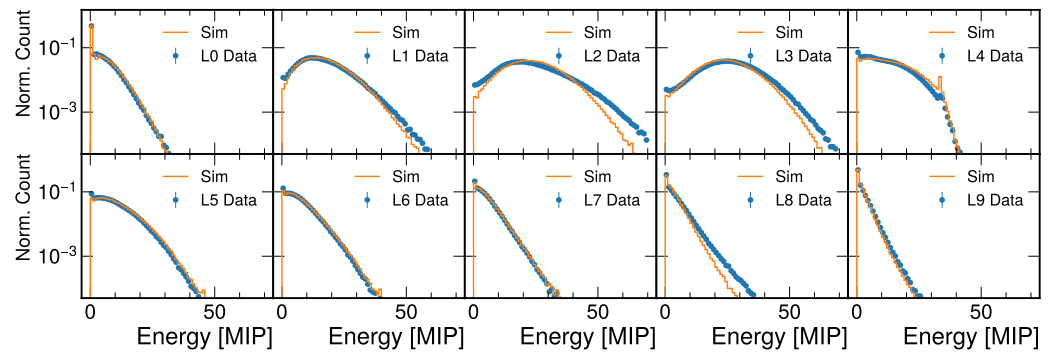


Figure 6. Total energy per layer.

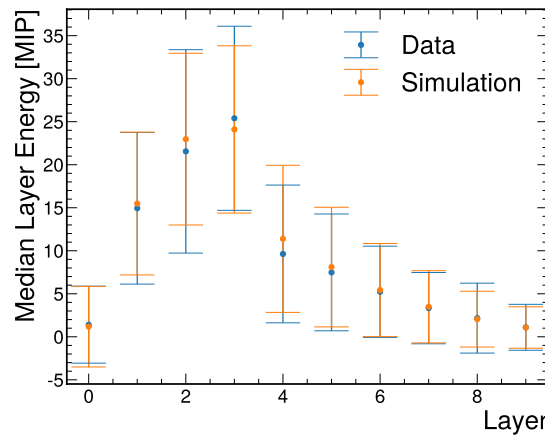


Figure 7. The median (markers) and RMS (error bar) of the energy distribution per each layer.

Figure 8 shows that the energy-weighted hit positions for each layer align reasonably well with the simulation. The x distributions suggest symmetric beam coverage along the x axis, spanning the entire prototype. Conversely, the y distributions reflect the beam experiencing a shift and tilt in the y direction. The central region between the two peak bins tends to flatten out as the sampling layers progress, as expected. As the simulation did not account for optical crosstalk, the agreement between the data and simulation is consistent with the notion that optical cross-talk is negligible in the data, as supported by our benchtop measurements [23]. However, it is important to note that the absence of a tracker in the setup that we used precludes further studies and definitive conclusions.

Finally, the total energy spectrum of the shower is shown in Figure 9. The simulation offers a reasonable approximation of the data, accurately capturing both its mean and standard deviation, which is driven by the spread of the beam energy. These discrepancies may arise from inherent challenges in precisely emulating beam conditions, potential miscalibration, or cell non-uniformity.

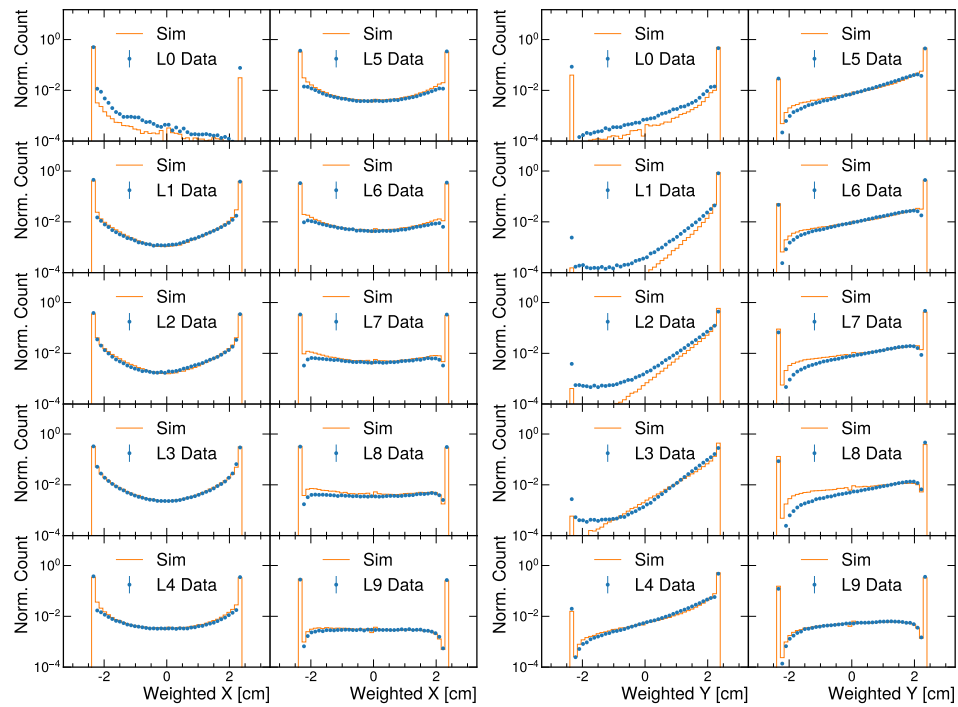


Figure 8. Energy-weighted x (left two columns) and y (right two columns) positions in each layer.

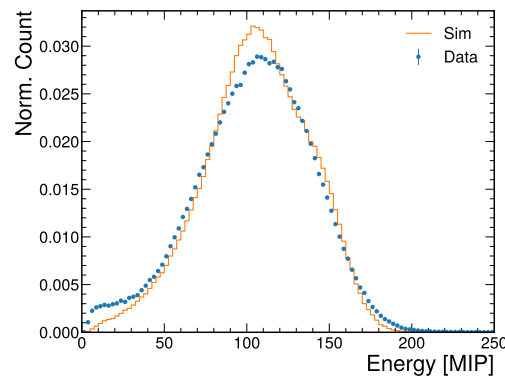


Figure 9. Total energy per shower.

6. Summary and Outlook

We conducted comprehensive studies on the first prototype for the EIC calorimeter insert [5], which is based on SiPM-on-tile technology. A proof-of-concept 40-channel prototype was built and tested using positron beams at Jefferson Laboratory. Key metrics such as energy spectra and 3D shower shapes were assessed, verified against simulations, and found to be in reasonable agreement.

Our test results suggest the potential feasibility of the proposed CALI design, which features an ASIC-away-from-SiPM/SiPM-on-tile strategy that uses megatiles defined by 3D-printed plastic frames. This strategy has the potential to reduce cooling needs and make more efficient usage of space while yielding negligible optical cross-talk.

The results reported here were obtained with a preliminary prototype featuring $O(1)\%$ of the channel count planned for the final detector. Nonetheless, our results aligns with the objectives, confirming key aspects of the CALI design. This work has resulted in improved construction methods and more clearly defined strategies for CALI’s operation and calibration.

Importantly, we have established a precedent by demonstrating the pioneering use of SiPM-on-tile technology for EIC detectors. This offers insights that could inform future studies of other EIC subdetectors, such as the forward hadronic calorimeter [33], the

zero-degree calorimeter, and the few-degree calorimeter [34], and may even extend to experiments beyond the EIC.

7. Code Availability

The simulation and analysis code used in this study is available on https://github.com/bschmookler/beamtests_dd4hep (accessed on 1 September 2023).

Author Contributions: Conceptualization, M.A.; Experimental Setup, B.B., S.P., S.J.P., J.H., P.C. and M.R.; Data Analysis, W.Z., S.J.P., S.P., J.H., P.C. and R.M.; Visualization, W.Z. and S.P.; Writing original draft, W.Z. and S.P.; Review & Editing, M.A. All authors have read and agreed to the published version of the manuscript.

Funding: This work was supported by the MRPI program of the University of California Office of the President, award number 00010100. This work is based on work supported by the U.S. Department of Energy, Office of Science, Office of Nuclear Physics, RENEW under Award Number DE-SC0022526, which supported Jiajun Huang and Miguel Rodriguez. Sebouh J. Paul acknowledges the support of the Jefferson Laboratory EIC Center Fellowship. Sean Preins was supported by a HEP-CAT fellowship from DOE award DE-SC0022313. Miguel Arratia acknowledges support through DOE Contract No. DE-AC05-06OR23177, under which Jefferson Science Associates, LLC operates the Thomas Jefferson National Accelerator Facility.

Data Availability Statement: The data presented in this study are available on request from the corresponding author.

Acknowledgments: We thank members of the California EIC consortium, in particular Oleg Tsai, for valuable feedback related to our design and studies. We thank Alexander Somov for his guidance during our test at Hall D and for his continued support afterward. We thank Ron Soltz and Ernst Sichtermann for supporting and guiding Jiajun Huang and Miguel Rodriguez.

Conflicts of Interest: The authors declare no conflict of interest.

References

1. Accardi, A.; Albacete, J.L.; Anselmino, M.; Armesto, N.; Aschenauer, E.C.; Bacchetta, A.; Boer, D.; Brooks, W.K.; Burton, T.; Chang, N.B.; et al. Electron Ion Collider: The Next QCD Frontier: Understanding the glue that binds us all. *Eur. Phys. J. A* **2016**, *52*, 268. [[CrossRef](#)]
2. Adkins, J.K.; Akiba, Y.; Albataineh, A.; Amaryan, M.; Arsene, I.C.; Gayoso, C.A.; Bae, J.; Bai, X.; Baker, M.D.; Bashkanov, M.; et al. Design of the ECCE Detector for the Electron Ion Collider. *arXiv* **2022**, arXiv:2209.02580.
3. Adam, J.; Adamczyk, L.; Agrawal, N.; Aidala, C.; Akers, W.; Alekseev, M.; Allen, M.M.; Ameli, F.; Angerami, A.; Antonioli, P.; et al. ATHENA detector proposal—A totally hermetic electron nucleus apparatus proposed for IP6 at the Electron-Ion Collider. *J. Instrum.* **2022**, *17*, P10019. [[CrossRef](#)]
4. Abdul Khalek, R.; Accardi, A.; Adam, J.; Adamiak, D.; Akers, W.; Albaladejo, M.; Al-Bataineh, A.; Alexeev, M.G.; Ameli, F.; Antonioli, P.; et al. Science Requirements and Detector Concepts for the Electron-Ion Collider: EIC Yellow Report. *Nucl. Phys. A* **2022**, *1026*, 122447. [[CrossRef](#)]
5. Arratia, M.; Barish, K.; Blanchard, L.; Huang, H.Z.; Ji, Z.; Karki, B.; Long, O.; Milton, R.; Paul, A.; Paul, S.J.; et al. A high-granularity calorimeter insert based on SiPM-on-tile technology at the future Electron-Ion Collider. *Nucl. Instrum. Meth. A* **2023**, *1047*, 167866. [[CrossRef](#)]
6. Blazey, G.; Chakraborty, D.; Dyshkant, A.; Francis, K.; Hedin, D.; Hill, J.; Lima, G.; Powell, J.; Salcido, P.; Zutshi, V.; et al. Directly Coupled Tiles as Elements of a Scintillator Calorimeter with MPPC Readout. *Nucl. Instrum. Meth. A* **2009**, *605*, 277–281. [[CrossRef](#)]
7. Simon, F.; Soldner, C. Uniformity Studies of Scintillator Tiles directly coupled to SiPMs for Imaging Calorimetry. *Nucl. Instrum. Meth. A* **2010**, *620*, 196–201. [[CrossRef](#)]
8. Sefkow, F.; White, A.; Kawagoe, K.; Pöschl, R.; Repond, J. Experimental tests of particle flow calorimetry. *Rev. Mod. Phys.* **2016**, *88*, 015003. [[CrossRef](#)]
9. Adloff, C.; Karyotakis, Y.; Repond, J.; Brandt, A.; Brown, H.; De, K.; Medina, C.; Smith, J.; Li, J.; Sosebee, M.; et al. Construction and Commissioning of the CALICE Analog Hadron Calorimeter Prototype. *J. Instrum.* **2010**, *5*, P05004. [[CrossRef](#)]
10. The CALICE Collaboration. Design, Construction and Commissioning of a Technological Prototype of a Highly Granular SiPM-on-tile Scintillator-Steel Hadronic Calorimeter. *arXiv* **2022**, arXiv:2209.15327.
11. CLICdp Collaboration. *Detector Technologies for CLIC*; CERN-2019-001; CERN: Geneva, Switzerland, 2019. [[CrossRef](#)]
12. The CEPC Study Group. CEPC Conceptual Design Report: Volume 2—Physics & Detector. *arXiv* **2018**, arXiv:1811.10545.
13. Li, L.; Shan, Q.; Jia, W.; Yu, B.; Liu, Y.; Shi, Y.; Hu, T.; Jiang, J. Optimization of the CEPC-AHCAL scintillator detector cells. *J. Instrum.* **2021**, *16*, P03001. [[CrossRef](#)]

14. Jiang, J.; Shi, Y.; Niu, Y.; Zhao, S.; Zhang, Y.; Liu, J.; Hu, T.; Liu, Y.; Yu, B. A study of sensitive elements of CEPC-AHCAL. *J. Instrum.* **2020**, *15*, C05041. [[CrossRef](#)]
15. Duan, Y.; Jiang, J.; Li, J.; Li, L.; Li, S.; Liu, D.; Liu, J.; Liu, Y.; Qi, B.; Qian, R.; et al. Scintillator tile batch test of CEPC AHCAL. *J. Instrum.* **2022**, *17*, P05006. [[CrossRef](#)]
16. Abramowicz, H.; Jovin, T.A.; Alonso, O.; Amjad, M.S.; An, F.; Andricek, L.; Anduze, M.; Anguiano, J.; Antonov, E.; Aoki, Y.; et al. International Large Detector: Interim Design Report. *arXiv* **2020**, arXiv:2003.01116.
17. Contardo, D.; Ball, A.; CMS Collaboration. The Phase-2 Upgrade of the CMS Endcap Calorimeter. Technical Report, CERN-LHCC-2017-023, CMS-TDR-019; CERN: Geneva, Switzerland, 2017.
18. Contardo, D.; Klute, M.; Mans, J.; Silvestris, L.; Butler, J. *Technical Proposal for the Phase-II Upgrade of the CMS Detector*; Technical Report, CERN-LHCC-2015-010; CERN: Geneva, Switzerland, 2015. [[CrossRef](#)]
19. Belloni, A.; Chen, Y.M.; Dyshkant, A.; Edberg, T.K.; Eno, S.; Freeman, J.; Krohn, M.; Lai, Y.; Lincoln, D.; Los, S.; et al. Test beam study of SiPM-on-tile configurations. *J. Instrum.* **2021**, *16*, P07022. [[CrossRef](#)]
20. Acar, B.; Adamov, G.; Adloff, C.; Afanasiev, S.; Akchurin, N.; Akgün, B.; Alhusseini, M.; Alison, J.; de Almeida, P.D.; Alpana, A.; et al. Performance of the CMS High Granularity Calorimeter prototype to charged pion beams of 20–300 GeV/c. *J. Instrum.* **2023**, *18*, P08014. [[CrossRef](#)]
21. Andreev, V.; Balagura, V.; Bobchenko, B.; Buzhan, P.; Cvach, J.; Danilov, M.; Devitsin, E.; Dodonov, V.; Dolgoshein, B.; Eigen, G.; et al. A high-granularity scintillator calorimeter readout with silicon photomultipliers. *Nucl. Instrum. Methods Phys. Res. Sect. Accel. Spectrometers Detect. Assoc. Equip.* **2005**, *540*, 368–380. [[CrossRef](#)]
22. Bombardi, G.; Marchioro, A.; Vergine, T.; Bouyjou, F.; Guilloux, F.; Callier, S.; Dulucq, F.; Berni, M.E.; de La Taille, C.; Raux, L.; et al. HGCROC-Si and HGCROC-SiPM: The front-end readout ASICs for the CMS HGCAL. In Proceedings of the 2020 IEEE Nuclear Science Symposium and Medical Imaging Conference (NSS/MIC), Boston, MA, USA, 31 October–7 November 2020; pp. 1–4.
23. Arratia, M.; Garabito Ruiz, L.; Huang, J.; Paul, S.J.; Preins, S.; Rodriguez, M. Studies of time resolution, light yield, and crosstalk using SiPM-on-tile calorimetry for the future Electron-Ion Collider. *J. Instrum.* **2023**, *18*, P05045. [[CrossRef](#)]
24. MPPC S14160-3015PS. Available online: https://www.hamamatsu.com/us/en/product/optical-sensors/mppc/mppc_mppc-array/S14160-3015PS.html (accessed on 23 August 2023).
25. Paul, S.J.; Arratia, M. Leveraging Staggered Tessellation for Enhanced Spatial Resolution in High-Granularity Calorimeters. *arXiv* **2023**, arXiv:2308.06939.
26. Adhikari, S.; Akondi, C.S.; Al Ghouli, H.; Ali, A.; Amaryan, M.; Anassontzis, E.G.; Austregesilo, A.; Barbosa, F.; Barlow, J.; Barnes, A.; et al. The GLUEX beamline and detector. *Nucl. Instrum. Meth. A* **2021**, *987*, 164807. [[CrossRef](#)]
27. Barbosa, F.; Hutton, C.; Sitnikov, A.; Somov, A.; Somov, S.; Tolstukhin, I. Pair spectrometer hodoscope for Hall D at Jefferson Lab. *Nucl. Instrum. Meth. A* **2015**, *795*, 376–380. [[CrossRef](#)]
28. Venaruzzo, M.; Abba, A.; Tintori, C.; Venturini, Y. FERS-5200: A distributed Front-End Readout System for multidetector arrays. *arXiv* **2020**, arXiv:2010.15688.
29. A5261—SiPM Remotization Cable (0.7 m) for A5253. Available online: <https://www.caen.it/products/a5261/> (accessed on 23 August 2023).
30. Frank, M.; Gaede, F.; Grefe, C.; Mato, P. DD4hep: A Detector Description Toolkit for High Energy Physics Experiments. *J. Phys. Conf. Ser.* **2014**, *513*, 022010. [[CrossRef](#)]
31. Agostinelli, S.; Allison, J.; Amako, K.A.; Apostolakis, J.; Araujo, H.; Arce, P.; Asai, M.; Axen, D.; Banerjee, S.; Barrand, G.J.N.I.; et al. GEANT4—a simulation toolkit. *Nucl. Instrum. Meth. A* **2003**, *506*, 250–303. [[CrossRef](#)]
32. de Silva, L.M.S.; Simon, F. Effects of misalignment on response uniformity of SiPM-on-tile technology for highly granular calorimeters. *J. Instrum.* **2020**, *15*, P06030. [[CrossRef](#)]
33. Bock, F.; Schmidt, N.; Wang, P.K.; Santiesteban, N.; Horn, T.; Huang, J.; Lajoie, J.; Camacho, C.M.; Adkins, J.K.; Akiba, Y.; et al. Design and Simulated Performance of Calorimetry Systems for the ECCE Detector at the Electron Ion Collider. *Nucl. Instrum. Meth. A* **2023**, *1055*, 168464. [[CrossRef](#)]
34. Arratia, M.; Milton, R.; Paul, S.J.; Schmookler, B.; Zhang, W. A Few-Degree Calorimeter for the future Electron-Ion Collider. *arXiv* **2023**, arXiv:2307.12531.

Disclaimer/Publisher’s Note: The statements, opinions and data contained in all publications are solely those of the individual author(s) and contributor(s) and not of MDPI and/or the editor(s). MDPI and/or the editor(s) disclaim responsibility for any injury to people or property resulting from any ideas, methods, instructions or products referred to in the content.